Draft version August 30, 2016
Preprint typeset using LaTeX style AASTeX6 v. 1.0

ACCRETION ONTO PROTO-BROWN DWARFS: MASS TRANSPORTATION IN THE DISK

L. C. Mayorga[1]
Department of Astronomy, New Mexico State University, Las Cruces, NM 88003-8001, USA

K. Kratter, J. Stone
Steward Observatory, University of Arizona, Tucson, AZ 85721, USA

[1]NSF GRFP Fellow

ABSTRACT

We present the results of our simple, semi-analytic, proto-brown dwarf disk simulations. Recent work has shown that brown dwarf disks may reach the same physical extent as proto-solar disks while potentially being of lower mass. To better understand the dominant mechanisms for mass transportation, the goal of this project is to time-evolve disks located around $0.07M_\odot < M < 1M_\odot$ central objects and include the effects of non-ideal magnetohydrodynamics, self gravity, and vertical shear on mass transportation. We discuss the effects of changing the host's mass as well as how environmental changes might affect mass transport.

1. INTRODUCTION

The definition of a brown dwarf has been hotly contested and debated. While the upper mass limit of brown dwarfs is reasonably well defined, the lower mass limit remains uncertain. Though some consider Deuterium-burning the hallmark of a brown dwarf, the differences between what makes a brown dwarf or a giant planet is inherently determined by the mechanisms of formation (Chabrier et al. 2014).

Brown dwarfs can occur in isolation, in binaries, and recent microlensing surveys are beginning to find brown dwarfs playing host to planet-sized objects (Udalski et al. 2015). The evidence points to brown dwarfs forming preferentially like stars rather than planets, through the gravitational collapse of a nebular cloud rather than via core accretion in a protoplanetary disk.

Initial proto-brown dwarf disk observations pointed to scaled down versions of protostellar disks, with maximum radii of 10–50 AU and masses up to a few M_J (Ricci et al. 2013; Scholz et al. 2006; Luhman et al. 2007). Radio observations with the Atacama Large Millimeter/sub-millimeter Array (ALMA) has determined that proto-brown dwarf disks are more similar to proto-stellar disks with radii near 100AU (Ricci et al. 2014). The masses of the disks are still relatively unknown due to uncertainties in the conversion of observed species to molecular hydrogen, which makes up the bulk of the disk mass.

The growth of a brown dwarf is determined by the accretion rate and is affected by how well mass is transported from the outer disk to the inner disk. Mass is transported inwards through angular momentum exchange and as a parcel falls inwards others are diffused outwards. Typically, disks are modeled as a diffusion problem where an effective viscosity, ν, is the outcome of turbulent processes rather than a molecular viscosity of gas (Armitage 2015).

The processes that generate turbulence and govern the formation of stars are reasonably well known. For gases, a multitude of instabilities have been previously studied and the following have been included in our simulations: magnetorotational instabilities (MRI) (Mohanty et al. 2013; Bai 2011; Bai & Goodman 2009; Igea & Glassgold 1999), gravitational or Toomre instabilities (GI) (Kratter et al. 2008), and vertical shear instabilities (VSI) (Lin & Youdin 2015). The inclusion of solids, in the form of dust, causes turbulence through other mechanisms such as the Kelvin-Helmholtz instability or the streaming instability (Armitage 2015).

For brown dwarf disks, whose properties are moderately uncertain, the strength and importance of these turbulent processes are not necessarily the same. The aforementioned instabilities vary in effectiveness, characterized by an effective α, with disk conditions. The smaller central object leads to a different amount of ionizing radiation, different velocities, temperatures, magnetic fields, etc.

In this report, we describe our simple, semi-analytic simulations to assess the effectiveness of various turbulent processes. By doing this, we can constrain how brown dwarf disks and their hosts evolve. Ultimately, we hope to determine observational characteristics that will differentiate between different formation channels influenced by environment or companions.

In SECTION 2 we describe our simulations and how they differ from previous work in detail. In SECTION 3 we describe our progress and discuss how our models differ from protostellar disk models. In SECTION 4 we conclude with what future work and explorations might be.

2. METHODS

To create our semi-analytic disk model, we follow the disk initial properties commonly used by viscous disk smiulations which are outlined by Bai (2011). The temperature,

$$T = 280 \left(\frac{a}{1\,\mathrm{AU}}\right)^{-\frac{1}{2}}\,\mathrm{K}, \tag{1}$$

and surface density,

$$\Sigma = 1700 \left(\frac{a}{1\,\mathrm{AU}}\right)^{-\frac{3}{2}}\,\mathrm{g\,cm^{-2}}, \tag{2}$$

scale smoothly with radius, a.

We have tested a variety of host masses, ranging from $0.07 - 1\ M_{\odot}$, sampled from Baraffe et al. (2015). From these evolution tables we can evolve the host object and track its radial growth and luminosity evolution with age. Given a host's mass, we can then compute the Keplerian frequency of the disk,

$$\Omega = \sqrt{\frac{GM_*}{a^3}}. \tag{3}$$

The sound speed in the disk is defined as,

$$c_s = \sqrt{\frac{kT}{\mu_n m_p}}, \tag{4}$$

where k is Boltzmann's constant, T is the disk temperature, $\mu_n = 2.34$, and m_p is the mass of a proton. The Keplerian frequency, in combination with the sound speed, allows us to compute the disk scale height,

$$H = \frac{c_s}{\Omega}, \tag{5}$$

as a function of disk radius. From this we can then calculate the density of the disk, ρ, as a function of disk radius and height above (and symmetrically below) the midplane, z, as follows:

$$\rho = \frac{\Sigma}{H\sqrt{2\pi}} \exp\left(\frac{-z^2}{2H^2}\right). \tag{6}$$

We have assumed a fixed magnetic field of $B = 1$ G for these simulations, but this could easily be modified to vary as a function of disk location. No direct measurements of the field strength in disks have been made aside from the remnants frozen into meteorites of 0.1–1 G (Levy & Sonett 1978). A lower limit of 10 mG has been considered from observations of Zeeman splitting of OH 18cm lines (Wardle 2007). Our field at 1 AU is not unreasonable for maintaining observationally inferred disk accretion rates (Calvet et al. 1999; Wardle 2007).

2.1. *Chemistry*

The magnetic field will act on charged species in the disk. Our simulations currently include neutral hydrogen and helium, free electrons, and HCO+ ions. The number densities of these species is of particular importance for calculating the effectiveness of different MRI terms. The ionizing radiation is predominantly from the amount of luminosity being released in X-rays.

There are three sources of ionizing radiation that have been identified as major contributers: stellar emission in X-rays, cosmic ray flux, and radioactive decay. The X-ray luminosity from the star is assumed to be a factor of $10^{3.5}$ reduced from the bolometric luminosity to match Mohanty et al. (2013). Appropriate time evolution of this quantity must also include an X-ray luminosity source from the accretion shock of mass falling onto the proto-brown dwarf, which we currently neglect.

The stellar ionization rate as a function of disk location, $\xi_X^{\rm eff}$, is then a function of the stellar X-ray emission, L_x, the distance from the proto-brown dwarf, R, and the column density of hydrogen nuclei above, N_{H1}, and below, N_{H2}. The ionization rate at that location can be written as follows:

$$\xi_X^{\rm eff} = \left(\frac{L_x}{10^{30}}\right)\left(\frac{1\,{\rm AU}}{R}\right)^{2.2}\left[\zeta_1(e^{-(N_{H1}/N_1)^\alpha} + e^{-(N_{H2}/N_1)^\alpha}) + \zeta_2(e^{-(N_{H1}/N_2)^\beta} + e^{-(N_{H2}/N_2)^\beta})\right]{\rm s}^{-1}, \tag{7}$$

where $N_1 = 3\times10^{21}\,{\rm cm}^{-2}$, $N_2 = 1\times10^{24}\,{\rm cm}^{-2}$, $\zeta_1 = 4\times10^{-11}$, $\zeta_2 = 2\times10^{-14}$, $\alpha = 0.5$, and $\beta = 0.7$ (Bai 2011).

The ionization rate from cosmic rays, unless shielded by stellar winds, takes the following form:

$$\xi_{\rm CR}^{\rm eff} = 2\times10^{-17}\exp\left(-\Sigma/96\,{\rm g\,cm}^{-2}\right)\,{\rm s}^{-1} \tag{8}$$

per hydrogen (Umebayashi & Nakano 1981). This rate is variable based on the proto-brown dwarf's environment. Observations of the cosmic ray flux toward the ζ Persei diffuse cloud, suggest a normalization factor of order $\sim 10^{-16}\,{\rm s}^{-1}$ (McCall et al. 2003). However, Bai & Goodman (2009) emphasized that cosmic rays have little effect on the inner regions of the disk, where we expect stellar sources of X-rays to dominate, and considered values from $0 - 10^{-15}\,{\rm s}^{-1}$ in their simulations.

Radioactive decay keeps the midplane of the disk from being fully neutral, but is generally too weak to provide sufficient ionization on its own. We adopt the ionization rate of $\xi_{\rm RD} = 10^{-19}{\rm s}^{-1}$ as suggested by Bai (2011). These are all combined into a single effective ionization rate, $\xi^{\rm eff} = \xi_X^{\rm eff} + \xi_{\rm CR}^{\rm eff} + \xi_{\rm RD}$, and we adopt the Igea & Glassgold (1999) method of determining an electron fraction,

$$x_e = n_e/n_H = \sqrt{\frac{\xi^{\rm eff}}{n_H\beta}}, \tag{9}$$

where $\beta = 2\times10^{-6}T^{-1/2}\,{\rm cm}^3\,{\rm s}^{-1}$ and n_H is the number density of hydrogen computed from $n_H, = \rho/(\mu_n m_p)$. We are currently assuming that the number density of electrons, n_e, is equivalent to the number of ions, n_i. Mohanty et al. (2013) identified the HCO+ ion as the most dominant molecular ion in their gas phase chemistry. For this reason, we have chosen to only consider H, He, and HCO+ in our simulations.

2.2. *Calculations of Magnetohydrodynamic (MHD) effects*

Magnetohydrodynamic (MHD) effects manifest themselves as magnetorotational instabilites (MRI). A weak vertical magnetic field can destabilize a Keplerian disk and cause radial perturbations. Consider two fluid parcels at the same radius coupled to an initially uniform vertical magnetic field. An initial perturbation radially will cause the two parcels to change their orbital velocity around the host object. This shear causes the inner parcel to move faster than the outer parcel and the parcels can pull the magnetic field line with them. Magnetic tension attempts to rectify the situation and results in a transfer of angular momentum from the inner parcel to the outer parcel causing the radial displacement between the two points to increase, leading to the instability.

Our calculation of the strength of the instability is dependent on the non-ideal MHD terms and follows the methodology of Bai (2011) which we reproduce here for convenience. In our discussion, the density and velocity of the neutral species are given by ρ, and $\boldsymbol{v}$, respectively. The charged species, j, have their own number density n_j, and drift velocity relative to the neutrals, $\boldsymbol{v}_j$. In the frame comoving with the neutrals, the equation of motion of the charged species is set by the equilibrium between the Lorentz force and neutral drag, given by

$$Z_j e\left(\boldsymbol{E}' + \frac{\boldsymbol{v}_j}{c}\times\boldsymbol{B}\right) = \gamma_j\rho m_j\boldsymbol{v}_j, \tag{10}$$

where $\boldsymbol{E}'$ is the electric field in the frame, the magnetic field, $\boldsymbol{B}$, is the same in all frames, and $\gamma \equiv \langle\sigma v\rangle_j/(m_n + m_j)$ with $\langle\sigma v\rangle_j$ being the rate coefficient for momentum transfer between the charged particles and the neutrals.

The momentum transfer rate coefficient for electrons is simply dependent on the temperature and we adopt

$$\langle\sigma v\rangle_e = 8.3\times10^{-9}\times\max\left[1, \left(\frac{T}{100{\rm K}}\right)^{1/2}\right]{\rm cm}^3\,{\rm s}^{-1} \tag{11}$$

as an approximation. For the ions, we adopt

$$\langle\sigma v\rangle_j = 2\times10^{-9}\left(\frac{m_H}{\mu}\right)^{1/2}\,{\rm cm}^3\,{\rm s}^{-1}, \tag{12}$$

where the reduced mass, $\mu = m_j m_n/(m_j + m_n)$. For completeness, we include the momentum transfer rate coefficient for grains despite them currently not being included in our simulations. We adopt

$$\langle \sigma v \rangle_{gr} = \max\left[1.3 \times 10^{-9}|Z|, 1.6 \times 10^{-7} \left(\frac{x}{1\,\mu\mathrm{m}}\right)^2 \left(\frac{T}{100\,\mathrm{K}}\right)^{1/2}\right] \mathrm{cm}^3\,\mathrm{s}^{-1}, \tag{13}$$

where x is the size of the grain particles in question.

The relative importance between the Lorentz force and neutral drag (Equation (10)) is characterized by the ratio between the gyrofrequency and the momentum exchange rate,

$$\beta_j \equiv \frac{Z_j e B}{m_j c} \frac{1}{\gamma_j \rho}. \tag{14}$$

The charged species is then strongly coupled to the neutrals if $|\beta_j| \ll 1$ and weakly coupled if $|\beta_j| \gg 1$.

The generalized Ohm's law can be obtained by inverting Equation (10) to solve for $\boldsymbol{v}_j$ and substituting the result into the equation for current density,

$$\boldsymbol{J} = \sigma_O \boldsymbol{E}'_{\parallel} + \sigma_H \hat{\boldsymbol{B}} \times \boldsymbol{E}'_{\perp} + \sigma_A \boldsymbol{E}'_{\perp}. \tag{15}$$

The three conductivities, Ohmic, Hall, and Pedersen conductivities are defined as follows:

$$\begin{aligned} \sigma_O &= \frac{ec}{B} \sum_j n_j Z_j \beta_j, \\ \sigma_H &= \frac{ec}{B} \sum_j \frac{n_j Z_j}{1 + \beta_j^2}, \\ \sigma_A &= \frac{ec}{B} \sum_j \frac{n_j Z_j \beta_j}{1 + \beta_j^2}, \end{aligned} \tag{16}$$

where σ_A, the Ambipolar term's magnetic conductivity, is usually written as σ_P, for Pedersen (Wardle 2007).

Ohm's Law, Equation (15), can be inverted to arrive at the induction equation,

$$\frac{\partial \boldsymbol{B}}{\partial t} = \nabla \times (\boldsymbol{v} \times \boldsymbol{B}) - \frac{4\pi}{c} \nabla \times \left[\eta_O \boldsymbol{J} + \eta_H (\boldsymbol{J} \times \hat{\boldsymbol{B}}) + \eta_A \boldsymbol{J}_{\perp}\right], \tag{17}$$

where the first term is the familiar induction term used for idealized MHD simulations, the second is the Ohmic diffusion term commonly seen in solar and stellar atmospheric simulations, the third is the Hall effect term, and the last is the Ambipolar diffusion term.

The magnetic diffusivities are defined as follows:

$$\begin{aligned} \eta_O &= \frac{c^2}{4\pi\sigma_O}, \\ \eta_H &= \frac{c^2}{4\pi\sigma_{\perp}} \frac{\sigma_H}{\sigma_{\perp}}, \\ \eta_A &= \frac{c^2}{4\pi\sigma_{\perp}} \frac{\sigma_A}{\sigma_{\perp}} - \eta_O, \end{aligned} \tag{18}$$

where $\sigma_{\perp} \equiv \sqrt{\sigma_H^2 + \sigma_A^2}$.

There are several things we should note from the aforementioned equations: 1) the Hall conductivity (seen in Equation (16)) depends on the sign of the charged species while the other two conductivities remain positive and thus may suppress or enhance the effects of MRI; 2) the absolute value of the diffusion coefficients (seen in Equation (18)) determines the relative importance of the various non-ideal MHD terms; and 3) if ions and electrons are the only charged species, which they currently are, then there is a relation between the Ohmic and Ambipolar diffusivities.

Physically, Ohmic diffusion dominates when the conductivity is low enough such that the field is imperfectly coupled to both the electrons and the ions. Essentially, the medium is not a perfect conductor. In a disk, Ohmic diffusion is dominant at high densities/low magnetic field strengths which are usually the innermost regions of the midplane in proto-solar disks.

Ambipolar diffusion dominates when the field is well-coupled to the ions and the electrons, thus the field drifts with the charged species relative to the neutral components of the disk. Regions of low densities/high field strengths are where Ambipolar diffusion is dominating and these regions are usually the furthest from protostar and at high altitudes.

The Hall effect operates best in the transitional regions, the midplane at intermediate distances from the host star, where the field is well-coupled to the electrons but imperfectly coupled to the ions. See Armitage (2011, 2015), Balbus & Terquem (2001), or Kunz & Balbus (2004) for much greater mathematical and conceptual discussion.

From the magnetic diffusivities (Equation (18)) it is useful to define a set of dimensionless numbers known as the Elsasser numbers or criteria:

$$\begin{aligned} \Lambda &\equiv \frac{v_A^2}{\eta_O \Omega}, \\ \chi &\equiv \frac{v_A^2}{\eta_H \Omega}, \\ Am &\equiv \frac{v_A^2}{\eta_A \Omega}, \end{aligned} \tag{19}$$

where the Alfvén velocity is defined as $v_A = \sqrt{B^2/4\pi\rho}$.

For the MRI to exist, the critical point is when the Elsasser number is greater than unity. If the Elsasser number is less than unity, the non-ideal MHD terms dominate over the inductive term and change the linear properties of the MRI substantially (Balbus & Terquem 2001; Kunz & Balbus 2004; Mohanty et al. 2013; Wardle 2007; Bai 2011). Once the dominant terms have been established for a particular region, MRI can then be invoked depending on the relevant criterion with a particular efficiency, $\alpha_{\rm MRI}$.

2.3. *Calculations of self-gravitation effects*

A self-gravitating disk is unstable to the growth of surface density perturbations. The parcels in the disk impart a gravitational force on other parcels and some initially stable regions can be perturbed such that the region can exceed the Jeans mass limit and collapse, forming a Toomre, or gravitational instability (GI). The angular momentum transport due to self-gravity may be dominant on large scales in young massive disks (Armitage 2015).

For GI, a simple analytic fit to simulation data has been compiled and computed from a number of sources by Kratter et al. (2008). They find that two components are required:

$$\alpha_{\rm GI} = \sqrt{\alpha_{\rm short}^2 + \alpha_{\rm long}^2}, \tag{20}$$

where the "short" component,

$$\alpha_{\rm short} = \max\left[0.14\left(\frac{1.3^2}{Q^2}\right)(1-\mu)^{1.15}, 0\right] \tag{21}$$

and the long component,

$$\alpha_{\rm long} = \max\left[\frac{1.4\times10^{-3}(2-Q)}{\mu^{5/4}Q^{1/2}}, 0\right] \tag{22}$$

dominate depending on disk thickness and the Toomre instability parameter,

$$Q = \frac{c_s \Omega}{\pi G \Sigma}. \tag{23}$$

2.4. *Calculations of entropic effects: Vertical Shear Instability (VSI)*

We defined our disk to have a radially dependent temperature gradient. At a particular cylindrical radius, the temperature gradient will vary as a function of height and cause a vertical shear. For VSI growth, the instability criterion is a cooling requirement,

$$t_{\rm cool} < \frac{h|q|}{\gamma - 1}\Omega^{-1}, \tag{24}$$

where h is the aspect ratio, q is the temperature power law, and γ is the adiabatic index. Typical values for these parameters are $h \sim 0.05$, $q \sim -0.5$, and $\gamma \simeq 1.4$ (Lin & Youdin 2015). The cooling timescale is then defined as

$$t_{\rm cool} = \frac{\Sigma c_s^2}{2\sigma T^4}. \tag{25}$$

Thus, the VSI will only operate in regions where cooling and heating processes results in the cooling time being shorter than the dynamical timescale, $1/\Omega$ (Armitage 2015). Lin & Youdin (2015) has shown that VSI operates mainly at

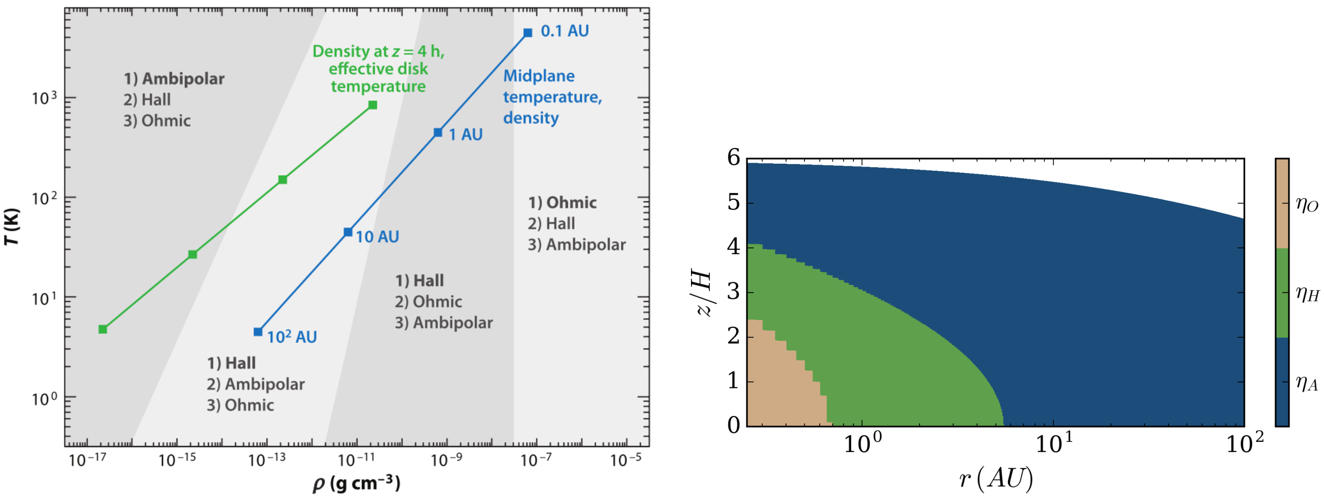

Figure 1. The dominant non-ideal MHD terms in a disk. Left from Armitage (2015): The relative importance of nonideal MHD terms is shown in the (ρ, T) plane (Balbus & Terquem 2001; Kunz & Balbus 2004), assuming a magnetic field strength such that $v_A/c_s = 0.1$. Also plotted are very approximate tracks showing the radial variation of physical conditions at the midplane, and near the surface, of protoplanetary disks. Right: The strongest MHD terms shown in the $(z/H,\, r)$ plane assuming a uniform magnetic field of 1 G.

intermediate radii, 5–50 AU, and its effectiveness can very with dust opacity changes. Numerical simulations suggest that $\alpha_{\rm VSI} \sim 10^{-4}$ (Nelson et al. 2013; Stoll & Kley 2014).

2.5. *Time Evolution*

A steady-state disk model neglects external torques and mass loss/gain. Time evolving the disk is then a matter of solving for the surface density as a function of radius and time, $\Sigma(r,t)$, such that it satisfies

$$\frac{\partial \Sigma}{\partial t} = \frac{3}{r}\frac{\partial}{\partial r}\left[r^{1/2}\frac{\partial}{\partial r}(\nu \Sigma r^{1/2})\right]. \tag{26}$$

The viscosity is taken to be

$$\nu = \alpha c_s H = \alpha \frac{c_s^2}{\Omega}, \tag{27}$$

where α is a mass transportation effectiveness computed from all the disk instabilities. The α-prescription varies from study to study as it must include all of the effects considered in each study. For a single effect, like GI, there are still several prescriptions in operation (Rafikov 2015).

In our case, our disks will be truly evolving with time and experiencing mass loss, accretion, and torques or angular momentum losses ($\dot{m}$, $\dot{M}$, $\dot{J}$). Thus the evolution equation gains a term

$$\frac{\partial \Sigma}{\partial t} = \frac{3}{r}\frac{\partial}{\partial r}\left[r^{1/2}\frac{\partial}{\partial r}(\nu \Sigma r^{1/2})\right] + \dot{\Sigma}(r,t). \tag{28}$$

3. PROGRESS/DISCUSSION

We have computed the initial conditions, with minimum ages given by Baraffe et al. (2015), of disks around protostars and proto-brown dwarfs ranging from $0.07 M_\odot < M < 1 M_\odot$. Our focus is to properly parametrize and reproduce the chemistry and MHD effects done by the previous studies of Mohanty et al. (2013) and Bai (2011) for proto-solar type stars before adjusting parameters to proto-brown dwarfs.

Figure 1 shows a comparison of the strength of the non-ideal MHD terms in a disk. The left panel is from Armitage (2015), for which the midplane conditions are estimated for a disk around a solar-mass star with $\Sigma = 10^3 (r/1\mathrm{AU})^{-1}\,\mathrm{g\,cm^{-2}}$. The surface conditions are estimated from the density at $z = \pm 4H$ (using a Gaussian density profile), assuming that the temperature is the effective temperature for a steady-state disk accreting at $\dot{M} = 10^{-7} M_\odot$ year^{-1}. For comparison, the right panel shows our disk around a solar-mass star with $\Sigma = 1700 (r/1\mathrm{AU})^{-3/2}\,\mathrm{g\,cm^{-2}}$ and is modeled up to $z = 6H$ with no accretion. Despite these differences, the dominant non-ideal terms exist in similar regions in the disk.

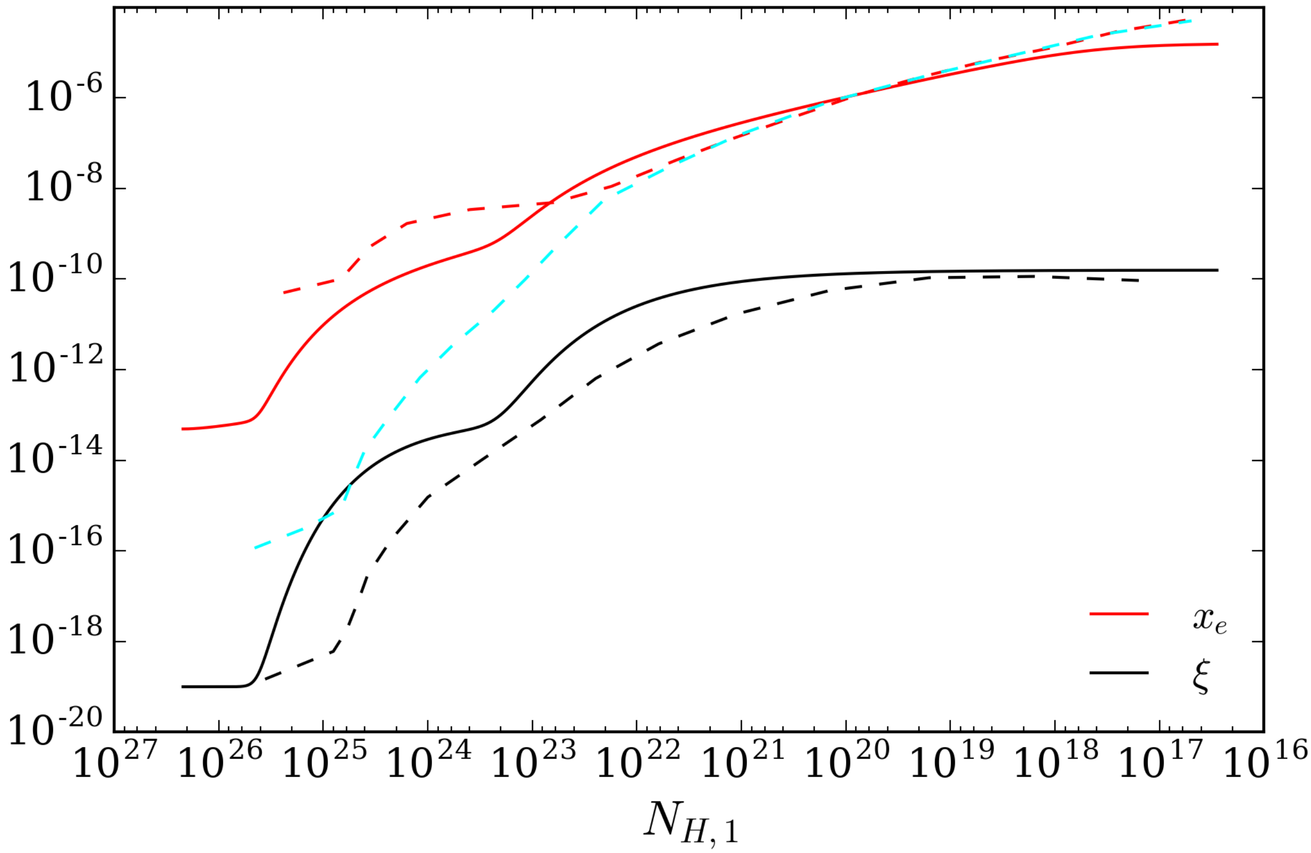

Figure 2. The effective ionization rate and ionization fractions as a function of column density compared with Mohanty et al. (2013) for a dustless disk at 1AU. The black line and red line is the ionization rate and electron/ion fraction of this work, respectively. The dashed black, cyan, and red lines are the ionization rate, electron fraction, and HCO+ fraction, respectively, from Mohanty et al. (2013).

In Figure 2, we compare our parametrization for the composition of a disk to the more chemically complex work of Mohanty et al. (2013). Despite our simplifications, the ionization rates and number densities are of appropriate order of magnitude. We have assumed that the number density of ions is equivalent to the number density of electrons which is not the case especially at higher column densities in the midplane. We intend to apply an efficiency function correction to our number densities to better match Mohanty et al. (2013).

The evolution of MRI with mass is of particular interest. Given varying ionization conditions, the disk will experience different amounts of X-ray radiation from the host object. The disk can then have a larger or smaller population of charged species to work with. Figure 3 shows how the regions where each non-ideal term dominates changes as a function of increasing host mass. Increasing the mass of the central object reduces the Keplerian frequency of the disk, Ω, which in turn increases the scale height, H. This changes the density profile of the disk and ultimately changes the ionizing radiation's ability to penetrate different regions of the disk. Consequently, there are more charged species, and the regions for which each effect dominates shifts outwards.

4. FUTURE WORK

We have demonstrated how a semi-analytic disk model can use simple parametrizations to replicate numerical simulations and approximate realistic disks. Yet, there is still much work to be done to improve our models and prepare them for comparison with disk observations.

- Include the X-ray luminosity from accretion shock

  Currently, the only host X-ray luminosity source is from bolometric contributions. The shock from material falling onto the proto-brown dwarf will inevitably be another source of X-rays that will ionize the inner regions of the disk.

- Apply efficiency correction to our n_e and n_i to better match Mohanty et al. (2013)

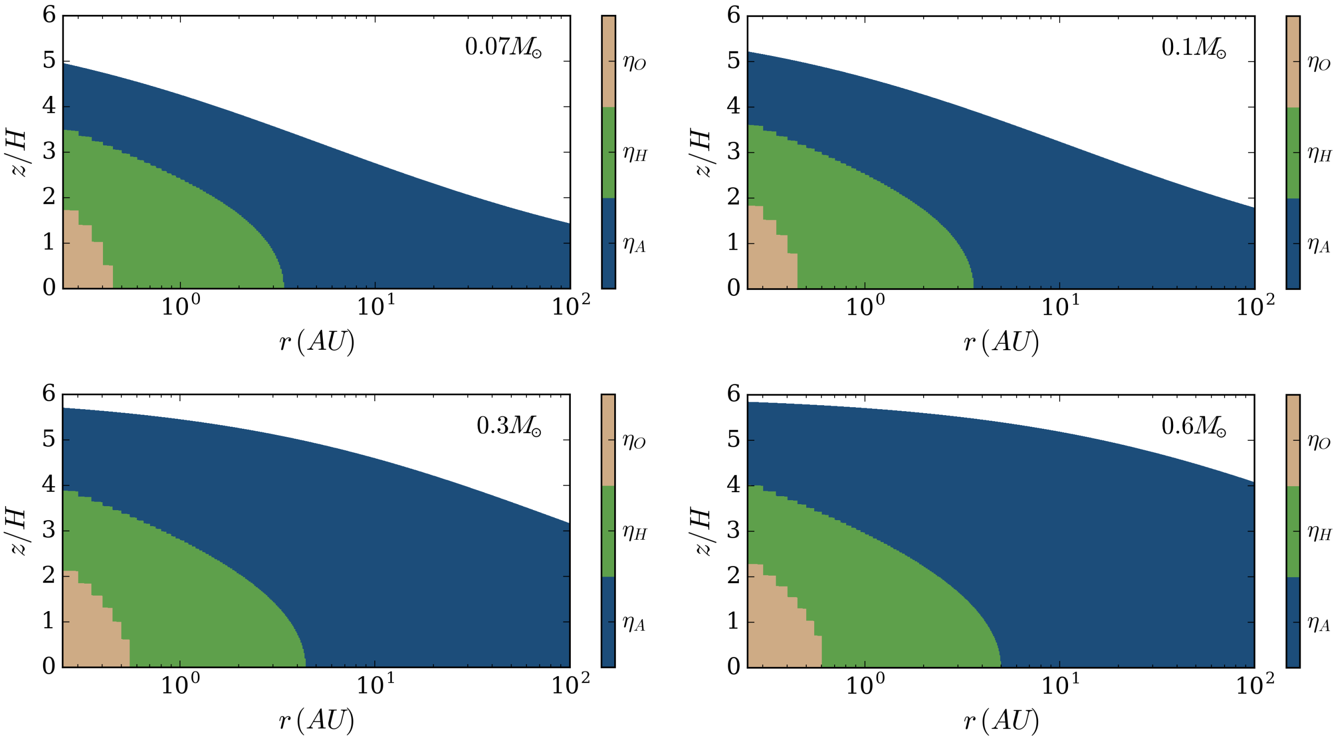

Figure 3. The dominant non-ideal MHD terms in a disk for various host object masses of $0.07M_\odot$ (upper left), $0.1M_\odot$ (upper right), $0.3M_\odot$ (lower left), and $0.6M_\odot$ (lower right).

Our simplification of the chemistry does not result in unreasonable number densities. However, we can do better and Mohanty et al. (2013) have carefully documented the number densities and ionization rates of their full chemical simulations. An efficiency function should be able to improve our match to their dustless and dusty cases.

- Turn on dust grains and implement dust coagulation ion deposition

  Currently, the dust grain portions of the MRI calculations are implemented in our simulation; but, for the sake of our initial simulations the dust calculations were not included. However, new physics is needed to include dust appropriately. Dust acts as a sink for other charged species due to the deposition of ions and electrons onto dust grains and the coagulation of dust particles. Another efficiency function for this process has yet to be implemented.

- Combined α-representations of mass transport

  There has been some work into computing the efficiency of the various instabilities, but how to best combine them is still somewhat uncertain. We have the efficiencies of GI and VSI, but MRI is treated somewhat differently by previous work. MRI is considered a binary switch, where at some combined Elsasser number MRI will switch on. This leads to the discussion of dead, undead, or even zombie zones (see a more careful discussion in Armitage (2015) or Mohanty et al. (2013)). A slightly different treatment or parametrization will be needed for MRI to properly combine with GI and VSI.

- Evolve disk in time

  Shown in this work are the initial conditions for our disks. The time evolution software has yet to be interfaced with these models, but with the completion of the aforementioned future work this portion is relatively straightforward.

- Explore disk environmental conditions

  Given the different environments in which we find brown dwarfs, we need to also model these different initial conditions. Cluster environments will have a higher cosmic ray ionization rate while isolated environments might have lower rates. Also, in binary situations the disk itself may lose mass to another object or experience torques that will inevitably affect mass transport in the disk and may hinder the growth of the proto-brown dwarf. Our models should be able to simulate these various environments.

- Compare disks with observations

  After exploring the parameter space of initial conditions, we will be able to compare our disks to observed disks and assess the validity of our models. We will also able to constrain how brown dwarfs evolve and provide observational characteristics that differentiate between various formation scenarios.

This work was initiated during the Kavli Summer Program in Astrophysics in 2016, hosted at the University of California, Santa Cruz. We would also like to thank S. Mohanty for his illuminating discussions on disk chemistry. In particular, L.C.M would like to thank her Kavli office mates for enlightening discussions and debugging assistance and would like to acknowledge support from the NSF GRFP. This material is based upon work supported by the National Science Foundation Graduate Research Fellowship Program under Grant No. DGE-1144458. Any opinions, findings, and conclusions or recommendations expressed in this material are those of the authors(s) and do not necessarily reflect the views of the National Science Foundation.

REFERENCES

Armitage, P. J. 2011, Annu. Rev. Astron. Astrophys., 49, 195
—. 2015, arXiv:1509.06382, 128
Bai, X.-N. 2011, ApJ, 739, 50
Bai, X.-N., & Goodman, J. 2009, ApJ, 701, 737
Balbus, S. A., & Terquem, C. 2001, ApJ, 552, 235
Baraffe, I., Homeier, D., Allard, F., & Chabrier, G. 2015, A&A, 577, A42
Calvet, N., Hartmann, L., & Strom, S. E. 1999, Protostars planets IV, 21
Chabrier, G., Johansen, A., Janson, M., & Rafikov, R. 2014, in Protostars Planets VI (University of Arizona Press)
Igea, J., & Glassgold, A. E. 1999, ApJ, 518, 848
Kratter, K. M. 2010, Doctor of philosophy, University of Toronto
Kratter, K. M., Matzner, C. D., & Krumholz, M. R. 2008, ApJ, 681, 375
Kunz, M. W., & Balbus, S. A. 2004, MNRAS, 348, 355
Levy, E. H., & Sonett, C. P. 1978, in Protostars Planets III, ed. T. Gehrels, 516–532
Lin, M.-K., & Youdin, A. N. 2015, ApJ, 811, 17
Luhman, K. L., Adame, L., D'Alessio, P., et al. 2007, ApJ, 666, 1219
McCall, B. J., Huneycutt, A. J., Saykally, R. J., et al. 2003, Nature, 422, 500
Mohanty, S., Ercolano, B., & Turner, N. J. 2013, ApJ, 764, 65
Nelson, R. P., Gressel, O., & Umurhan, O. M. 2013, MNRAS, 435, 2610
Rafikov, R. R. 2015, ApJ, 804, 62
Ricci, L., Isella, A., Carpenter, J. M., & Testi, L. 2013, ApJ, 764, L27
Ricci, L., Testi, L., Natta, A., et al. 2014, ApJ, 791, 20
Scholz, A., Jayawardhana, R., & Wood, K. 2006, ApJ, 645, 1498
Stoll, M. H. R., & Kley, W. 2014, A&A, 572, A77
Udalski, A., Jung, Y. K., Han, C., et al. 2015, ApJ, 812, 47
Umebayashi, T., & Nakano, T. 1981, PASJ, 33, 617
Wardle, M. 2007, Astrophys. Space Sci., 311, 35